Biomedical Optics EXPRESS

Characterizing relationship between optical microangiography signals and capillary flow using microfluidic channels

Woo June Choi,[1,3] Wan Qin,[1,3] Chieh-Li Chen,[1] Jingang Wang,[1] Qinqin Zhang,[1] Xiaoqi Yang,[2] Bruce Z. Gao,[2] and Ruikang K. Wang[1,*]

[1]*Department of Bioengineering, University of Washington, 3720 15th NE, Seattle, WA 98195, USA*
[2]*Department of Bioengineering and COMSET, Clemson University, Clemson, SC 29634, USA*
[3]*These authors contributed equally to this work*
[*]*wangrk@uw.edu*

Abstract: Optical microangiography (OMAG) is a powerful optical angiographic tool to visualize micro-vascular flow *in vivo*. Despite numerous demonstrations for the past several years of the qualitative relationship between OMAG and flow, no convincing quantitative relationship has been proven. In this paper, we attempt to quantitatively correlate the OMAG signal with flow. Specifically, we develop a simplified analytical model of the complex OMAG, suggesting that the OMAG signal is a product of the number of particles in an imaging voxel and the decorrelation of OCT (optical coherence tomography) signal, determined by flow velocity, inter-frame time interval, and wavelength of the light source. Numerical simulation with the proposed model reveals that if the OCT amplitudes are correlated, the OMAG signal is related to a total number of particles across the imaging voxel cross-section per unit time (flux); otherwise it would be saturated but its strength is proportional to the number of particles in the imaging voxel (concentration). The relationship is validated using microfluidic flow phantoms with various preset flow metrics. This work suggests OMAG is a promising quantitative tool for the assessment of vascular flow.

OCIS codes: (170.4500) Optical coherence tomography; (170.2655) Functional monitoring and imaging; (220.4000) Microstructure fabrication

References and links

1. D. Huang, E. A. Swanson, C. P. Lin, J. S. Schuman, W. G. Stinson, W. Chang, M. R. Hee, T. Flotte, K. Gregory, C. A. Puliafito, and et, "Optical coherence tomography," Science **254**(5035), 1178–1181 (1991).
2. W. Drexler and J. G. Fujimoto, "State-of-the-art retinal optical coherence tomography," Prog. Retin. Eye Res. **27**(1), 45–88 (2008).
3. S. Rofagha, R. B. Bhisitkul, D. S. Boyer, S. R. Sadda, and K. Zhang; SEVEN-UP Study Group, "Seven-year outcomes in ranibizumab-treated patients in ANCHOR, MARINA, and HORIZON: a multicenter cohort study (SEVEN-UP)," Ophthalmology **120**(11), 2292–2299 (2013).
4. S. Alam, R. J. Zawadzki, S. Choi, C. Gerth, S. S. Park, L. Morse, and J. S. Werner, "Clinical application of rapid serial fourier-domain optical coherence tomography for macular imaging," Ophthalmology **113**(8), 1425–1431 (2006).
5. D. M. Brown, Q. D. Nguyen, D. M. Marcus, D. S. Boyer, S. Patel, L. Feiner, P. G. Schlottmann, A. C. Rundle, J. Zhang, R. G. Rubio, A. P. Adamis, J. S. Ehrlich, and J. J. Hopkins; RIDE and RISE Research Group, "Long-term outcomes of ranibizumab therapy for diabetic macular edema: the 36-month results from two phase III trials: RISE and RIDE," Ophthalmology **120**(10), 2013–2022 (2013).
6. M. D. Davis, S. B. Bressler, L. P. Aiello, N. M. Bressler, D. J. Browning, C. J. Flaxel, D. S. Fong, W. J. Foster, A. R. Glassman, M. E. Hartnett, C. Kollman, H. K. Li, H. Qin, and I. U. Scott; Diabetic Retinopathy Clinical Research Network Study Group, "Comparison of time-domain OCT and fundus photographic assessments of retinal thickening in eyes with diabetic macular edema," Invest. Ophthalmol. Vis. Sci. **49**(5), 1745–1752 (2008).

#265340 Received 24 May 2016; revised 15 Jun 2016; accepted 15 Jun 2016; published 20 Jun 2016

7. P. V. Le, X. Zhang, B. A. Francis, R. Varma, D. S. Greenfield, J. S. Schuman, N. Loewen, and D. Huang; Advanced Imaging for Glaucoma Study Group, "Advanced imaging for glaucoma study: design, baseline characteristics, and inter-site comparison," Am. J. Ophthalmol. **159**(2), 393–403 (2015).
8. C. K. Leung, "Diagnosing glaucoma progression with optical coherence tomography," Curr. Opin. Ophthalmol. **25**(2), 104–111 (2014).
9. R. K. Wang, S. L. Jacques, Z. Ma, S. Hurst, S. R. Hanson, and A. Gruber, "Three dimensional optical angiography," Opt. Express **15**(7), 4083–4097 (2007).
10. A. Zhang, Q. Zhang, C.-L. Chen, and R. K. Wang, "Methods and algorithms for optical coherence tomography-based angiography: a review and comparison," J. Biomed. Opt. **20**(10), 100901 (2015).
11. R. F. Spaide, J. M. Klancnik, Jr., and M. J. Cooney, "Retinal vascular layers imaged by fluorescein angiography and optical coherence tomography angiography," JAMA Ophthalmol. **133**(1), 45–50 (2015).
12. A. Mariampillai, B. A. Standish, E. H. Moriyama, M. Khurana, N. R. Munce, M. K. Leung, J. Jiang, A. Cable, B. C. Wilson, I. A. Vitkin, and V. X. D. Yang, "Speckle variance detection of microvasculature using swept-source optical coherence tomography," Opt. Lett. **33**(13), 1530–1532 (2008).
13. J. Enfield, E. Jonathan, and M. Leahy, "*In vivo* imaging of the microcirculation of the volar forearm using correlation mapping optical coherence tomography (cmOCT)," Biomed. Opt. Express **2**(5), 1184–1193 (2011).
14. Y. Jia, O. Tan, J. Tokayer, B. Potsaid, Y. Wang, J. J. Liu, M. F. Kraus, H. Subhash, J. G. Fujimoto, J. Hornegger, and D. Huang, "Split-spectrum amplitude-decorrelation angiography with optical coherence tomography," Opt. Express **20**(4), 4710–4725 (2012).
15. S. Zotter, M. Pircher, T. Torzicky, M. Bonesi, E. Götzinger, R. A. Leitgeb, and C. K. Hitzenberger, "Visualization of microvasculature by dual-beam phase-resolved Doppler optical coherence tomography," Opt. Express **19**(2), 1217–1227 (2011).
16. D. Y. Kim, J. Fingler, J. S. Werner, D. M. Schwartz, S. E. Fraser, and R. J. Zawadzki, "*In vivo* volumetric imaging of human retinal circulation with phase-variance optical coherence tomography," Biomed. Opt. Express **2**(6), 1504–1513 (2011).
17. R. K. Wang, L. An, P. Francis, and D. J. Wilson, "Depth-resolved imaging of capillary networks in retina and choroid using ultrahigh sensitive optical microangiography," Opt. Lett. **35**(9), 1467–1469 (2010).
18. M. R. Thorell, Q. Zhang, Y. Huang, L. An, M. K. Durbin, M. Laron, U. Sharma, P. F. Stetson, G. Gregori, R. K. Wang, and P. J. Rosenfeld, "Swept-source OCT angiography of macular telangiectasia type 2," Ophthalmic Surg. Lasers Imaging Retina **45**(5), 369–380 (2014).
19. Q. Zhang, C. S. Lee, J. Chao, C. L. Chen, T. Zhang, U. Sharma, A. Zhang, J. Liu, K. Rezaei, K. L. Peeple, R. Munsen, J. Kinyoun, M. Johnstone, R. N. Van Gelder, and R. K. Wang,"Wide-field optical coherence tomography based microanigography for retinal imaging," Sci. Rep. **6**(22017), (2016).
20. L. Roisman, Q. Zhang, R. K. Wang, G. Gregori, A. Zhang, C. L. Chen, M. K. Durbin, L. An, P. F. Stetson, G. Robbins, A. Miller, F. Zeng, and P. J. Rosenfeld, "Optical coherence tomography angiography of asymptomatic neovascularization in intermediated age-related macular degeneration," Ophthalmology **123**, 1309–1319 (2016).
21. Y. Winetraub, E. D. SoRelle, O. Liba, and A. de la Zerda, "Quantitative contrast-enhanced optical coherence tomography," Appl. Phys. Lett. **108**(2), 023702 (2016).
22. L. An, J. Qin, and R. K. Wang, "Ultrahigh sensitive optical microangiography for *in vivo* imaging of microcirculations within human skin tissue beds," Opt. Express **18**(8), 8220–8228 (2010).
23. T. Durduran, R. Choe, W. B. Baker, and A. G. Yodh, "Diffuse optics for tissue monitoring and tomography," Rep. Prog. Phys. **73**(7), 076701 (2010).
24. J. W. Goodman, "Statistical optics," New York, Wiley-Interscience, 1985, 567 p. **1** (1985).
25. Y. Wang and R. K. Wang, "Measurement of particle concentration in flow by statistical analyses of optical coherence tomography signals," Opt. Lett. **36**(11), 2143–2145 (2011).
26. V. M. Kodach, D. J. Faber, J. van Marle, T. G. van Leeuwen, and J. Kalkman, "Determination of the scattering anisotropy with optical coherence tomography," Opt. Express **19**(7), 6131–6140 (2011).
27. Q. Zhang, Y. Huang, T. Zhang, S. Kubach, L. An, M. Laron, U. Sharma, and R. K. Wang, "Wide-field imaging of retinal vasculature using optical coherence tomography-based microangiography provided by motion tracking," J. Biomed. Opt. **20**(6), 066008 (2015).
28. W. Qin, U. Baran, and R. Wang, "Lymphatic response to depilation-induced inflammation in mouse ear assessed with label-free optical lymphangiography," Lasers Surg. Med. **47**(8), 669–676 (2015).
29. S. M. Kazmi, E. Faraji, M. A. Davis, Y. Y. Huang, X. J. Zhang, and A. K. Dunn, "Flux or speed? Examining speckle contrast imaging of vascular flows," Biomed. Opt. Express **6**(7), 2588–2608 (2015).
30. V. J. Srinivasan, H. Radhakrishnan, E. H. Lo, E. T. Mandeville, J. Y. Jiang, S. Barry, and A. E. Cable, "OCT methods for capillary velocimetry," Biomed. Opt. Express **3**(3), 612–629 (2012).
31. Y. Li, U. Baran, and R. K. Wang, "Application of thinned-skull cranial window to mouse cerebral blood flow imaging using optical microangiography," PLoS One **9**(11), e113658 (2014).
32. J. Tokayer, Y. Jia, A.-H. Dhalla, and D. Huang, "Blood flow velocity quantification using split-spectrum amplitude-decorrelation angiography with optical coherence tomography," Biomed. Opt. Express **4**(10), 1909–1924 (2013).
33. G. Liu, W. Jia, V. Sun, B. Choi, and Z. Chen, "High-resolution imaging of microvasculature in human skin in-vivo with optical coherence tomography," Opt. Express **20**(7), 7694–7705 (2012).
34. Y. Jia, P. Li, and R. K. Wang, "Optical microangiography provides an ability to monitor responses of cerebral microcirculation to hypoxia and hyperoxia in mice," J. Biomed. Opt. **16**(9), 096019 (2011).

#265340 Received 24 May 2016; revised 15 Jun 2016; accepted 15 Jun 2016; published 20 Jun 2016

35. E. Wei, Y. Jia, O. Tan, B. Potsaid, J. J. Liu, W. Choi, J. G. Fujimoto, and D. Huang, "Parafoveal retinal vascular response to pattern visual stimulation assessed with OCT angiography," PLoS One **8**(12), e81343 (2013).
36. M. Unekawa, M. Tomita, Y. Tomita, H. Toriumi, K. Miyaki, and N. Suzuki, "RBC velocities in single capillaries of mouse and rat brains are the same, despite 10-fold difference in body size," Brain Res. **1320**, 69–73 (2010).
37. Y. Pan, R. Birngruber, J. Rosperich, and R. Engelhardt, "Low-coherence optical tomography in turbid tissue: theoretical analysis," Appl. Opt. **34**(28), 6564–6574 (1995).
38. G. Fuchsjäger-Mayrl, B. Wally, M. Georgopoulos, G. Rainer, K. Kircher, W. Buehl, T. Amoako-Mensah, H. G. Eichler, C. Vass, and L. Schmetterer, "Ocular blood flow and systemic blood pressure in patients with primary open-angle glaucoma and ocular hypertension," Invest. Ophthalmol. Vis. Sci. **45**(3), 834–839 (2004).
39. K. Yaoeda, M. Shirakashi, S. Funaki, H. Funaki, T. Nakatsue, and H. Abe, "Measurement of microcirculation in the optic nerve head by laser speckle flowgraphy and scanning laser Doppler flowmetry," Am. J. Ophthalmol. **129**(6), 734–739 (2000).
40. V. Doblhoff-Dier, L. Schmetterer, W. Vilser, G. Garhöfer, M. Gröschl, R. A. Leitgeb, and R. M. Werkmeister, "Measurement of the total retinal blood flow using dual beam Fourier-domain Doppler optical coherence tomography with orthogonal detection planes," Biomed. Opt. Express **5**(2), 630–642 (2014).
41. C.-L. Chen, K. D. Bojikian, C. Xin, J. C. Wen, D. Gupta, Q. Zhang, R. C. Mudumbai, M. A. Johnstone, P. P. Chen, and R. K. Wang, "Repeatability and reproducibility of optic nerve head perfusion measurements using optical coherence tomography angiography," J. Biomed. Opt. **21**(6), 065002 (2016).
42. Z. Chu, J. Lin, C. Gao, C. Xin, Q. Zhang, C. L. Chen, L. Roisman, G. Gregori, P. J. Rosenfeld, and R. K. Wang, "Quantitative assessment of the retinal microvasculature using optical coherence tomography angiography," J. Biomed. Opt. **21**(6), 066008 (2016).
43. Y. Jia, S. T. Bailey, T. S. Hwang, S. M. McClintic, S. S. Gao, M. E. Pennesi, C. J. Flaxel, A. K. Lauer, D. J. Wilson, J. Hornegger, J. G. Fujimoto, and D. Huang, "Quantitative optical coherence tomography angiography of vascular abnormalities in the living human eye," Proc. Natl. Acad. Sci. U.S.A. **112**(18), E2395–E2402 (2015).
44. Q. Zhang, R. K. Wang, C. L. Chen, A. D. Legarreta, M. K. Durbin, L. An, U. Sharma, P. F. Stetson, J. E. Legarreta, L. Roisman, G. Gregori, and P. J. Rosenfeld, "Swept source optical coherence tomography angiography of neovascular macular telangiectasia type 2," Retina **35**(11), 2285–2299 (2015).
45. P. Bedggood and A. Metha, "Direct visualization and characterization of erythrocyte flow in human retinal capillaries," Biomed. Opt. Express **3**(12), 3264–3277 (2012).
46. L. Shi, J. Qin, R. Reif, and R. K. Wang, "Wide velocity range Doppler optical microangiography using optimized step-scanning protocol with phase variance mask," J. Biomed. Opt. **18**(10), 106015 (2013).
47. T. Klein, W. Wieser, L. Reznicek, A. Neubauer, A. Kampik, and R. Huber, "Multi-MHz retinal OCT," Biomed. Opt. Express **4**(10), 1890–1908 (2013).

1. Introduction

Optical coherence tomography (OCT) can provide *in vivo* cross-sectional image of a living sample with microscopic resolution [1,2]. Because of its non-contact, non-invasiveness and high resolution characteristics, OCT has become the most widely used optical technique in medical imaging. Especially, this technology has increasingly become a standard of care in ophthalmic imaging for the diagnosis and management of several ocular conditions and diseases such as age-related macular degeneration (AMD) [3,4], diabetic retinopathy [5,6] and glaucoma [7,8].

The recent advent of OCT angiography (OCTA) has made its development from a structural to a functional imaging modality [10]. OCTA is an extension of OCT to visualize blood flow within microcirculatory tissue beds *in vivo*. It essentially operates by separating the scattered light signals due to randomly moving particles, such as red blood cells (RBCs) within functional vessels, from the scattered signals due to surrounding static tissue [9,10]. OCTA can provide label-free, three-dimensional (3D) *in vivo* ocular blood flow imaging, permitting non-invasive, functional visualization of retinal and choroidal vasculatures [11]. There are several OCTA techniques currently available on Fourier domain OCT systems. In general, OCTA techniques can be classified into three categories by the signal information used to contrast flow: intensity (or amplitude), phase, and complex signal. The intensity-based OCTA generates flow signals by detecting the variance [12], correlation [13], and decorrelation [14] in the time-varying OCT speckle intensities. One advantage of the intensity-based OCTA is that it is relatively less sensitive to the phase noise. However, it may sometimes miss the opportunity to sense changes in the phase signal caused by flow. Doppler OCT [15] and phase variance OCT (pvOCT) [16] utilize the phase changes caused by blood flow to contrast flow signals. The phase-based OCTA is more sensitive to the small changes

#265340 Received 24 May 2016; revised 15 Jun 2016; accepted 15 Jun 2016; published 20 Jun 2016

in phase, thus is easily affected by the Doppler phase shift caused by bulk tissue motion; it therefore requires precise removal of bulk-motion from the retinal tissue.

Previously, we developed a novel optical microangiography (OMAG) for OCTA imaging [17]. OMAG employs a differential operation based on complex OCT signals to utilize both intensity and phase information available in the system; hence it is a complex-based OCTA technique. In the past several years, OMAG has been successful in identifying disorder or dysfunction in the retinal and choroidal microvascular networks *in vivo* [18–20]. Despite many promising results of ocular blood flow using OMAG, the quantitative relationship between OMAG and flow remains unclear. Understanding the relationship between OMAG and flow is imperative for quantitative ocular blood flow measurement, upon which the dynamics in retinal blood flow could be assessed with the flow parameters derived from the measured OMAG signals.

The purpose of this study is to determine the relationship between OMAG measurement and flow. We hypothesize that the OMAG signal reflects the flux of blood flow, that is, the total number of blood cells passing through the imaging voxel area per unit time, and thus its magnitude would vary mainly with blood flow velocity and hematocrit. To test this hypothesis, we developed an analytical model of the complex OMAG signal, from which the relationships between OMAG signal and flow are numerically derived with various flow metrics. The simulated results are then experimentally tested with the OMAG measurements of a microfluidic flow phantom with varying preset flow parameters. Correlation of the simulation and experimental results are presented here, and practicality of the quantitative OMAG in ophthalmology and neuroscience is discussed.

2. Theory

2.1 Analytical model of OMAG signal

To evaluate the relationship between OMAG and flow, a fundamental understanding of OMAG signal is needed. To interpret the OMAG signal, we propose a simplified analytical model of OMAG. We start with a complex OCT signal obtained at a particular depth position of a dynamic scattering medium. For simplicity, we do not take into the consideration of the DC, mutual cross-correlation, and noise components in the OCT signal formulation because they are not relevant to our discussion. The OCT signal can be described as the superposition of all the light fields reflected from the scatters within an imaging voxel (coherent volume) in the medium [21]. Because the light field is treated as a vector of magnitude and angle (phasor) that are time-variant due to a random arrangement of the scattering particles within the imaging voxel, the OCT signal can be expressed as a sum of many random phasors as

$$\tilde{A}(t) = A(t)e^{i\phi(t)}, \tag{1}$$

where $A(t)$ and $\phi(t)$ are the time-varying random amplitude and angle of the resultant phasor, respectively. Recalling the principle of complex OMAG [22], it is described as an absolute difference between two adjacent complex-valued OCT B-frames captured at one location with a time interval ΔT, given by

$$\begin{aligned} I_{OMAG} &= \left| \tilde{A}(t+\Delta T) - \tilde{A}(t) \right| \\ &= \left| A(t+\Delta T)e^{i\phi(t+\Delta T)} - A(t)e^{i\phi(t)} \right|. \end{aligned} \tag{2}$$

Using a conjugate of the complex value, Eq. (2) can be rewritten as

#265340 Received 24 May 2016; revised 15 Jun 2016; accepted 15 Jun 2016; published 20 Jun 2016

$$
\begin{aligned}
I_{OMAG} &= \left| A(t+\Delta T)e^{i\phi(t+\Delta T)} - A(t)e^{i\phi(t)} \right| \\
&= \sqrt{\left(A(t+\Delta T)e^{i\phi(t+\Delta T)} - A(t)e^{i\phi(t)} \right) \cdot \left(A(t+\Delta T)e^{i\phi(t+\Delta T)} - A(t)e^{i\phi(t)} \right)^*} \\
&= \sqrt{A(t)^2 + A(t+\Delta T)^2 - 2A(t)A(t+\Delta T)\cos(\Delta\phi(t))},
\end{aligned} \tag{3}
$$

where $\Delta\phi(t)$ is the difference between the two random phases in $\tilde{A}(t)$ and $\tilde{A}(t+\Delta T)$. By dividing the term in the square root by $A(t)^2 + A(t+\Delta T)^2$, the Eq. (3) is given as

$$
I_{OMAG} = \sqrt{\left(A(t)^2 + A(t+\Delta T)^2 \right)\left[1 - \frac{2A(t)A(t+\Delta T)}{A(t)^2 + A(t+\Delta T)^2}\cos(\Delta\phi(t)) \right]}. \tag{4}
$$

the term in the square bracket of Eq. (4) denotes the decorrelation. Inspecting further, we can see that the second term in the decorrelation takes a normalized electric field autocorrelation function $g_1(\tau) = \langle A(t+\tau)A(t) \rangle / \langle A(t)A(t) \rangle$. Thus, Eq. (4) can be expressed as

$$
I_{OMAG} = \sqrt{\left(A(t)^2 + A(t+\Delta T)^2 \right)\left[1 - g_1(\Delta T)\cos(\Delta\phi(t)) \right]}. \tag{5}
$$

Assuming the scatters are independent with isotropic dynamics, $g_1(\Delta T)$ is given by [23]

$$
\left| g_1(\Delta T) \right|^2 = \exp\left(-8k^2 \left\langle \Delta r^2(\Delta T) \right\rangle / 6 \right). \tag{6}
$$

where, $k = 2\pi / \lambda_0$; λ_0 the center wavelength of OCT light source and $\left\langle \Delta r^2(\Delta T) \right\rangle$ is the mean-square displacement of the scatter in the time interval ΔT. For the directional flow with a Gaussian velocity distribution, $\left\langle \Delta r^2(\Delta T) \right\rangle = \left\langle V^2 \right\rangle \Delta T^2$, where $\left\langle V^2 \right\rangle$ is the second moment of the velocity distribution. Thus, the Eq. (5) can be rearranged with the flow velocity and the time interval in $g_1(\Delta T)$:

$$
I_{OMAG} = \sqrt{\left(A(t)^2 + A(t+\Delta T)^2 \right)\left[1 - \left[\exp\left(-\frac{8}{6}\left(\frac{2\pi}{\lambda_0} \right)^2 \left\langle V^2 \right\rangle \Delta T^2 \right) \right]^{1/2} \times \cos(\Delta\phi(t)) \right]}. \tag{7}
$$

According to Winertraub *et al*. [21], with the simplified assumptions: 1) single scattering regime, 2) reflections modeled by ray optics and 3) all particles having the same reflectance in the imaging voxel, the OCT signal detected from the scattering particle is proportional to a square root of the number of particles (*N*) within the imaging voxel that is given by [21]

$$
A(N)^2 = 0.89\alpha\sqrt{N} \qquad N \geq 2. \tag{8}
$$

where α is the backscattering coefficient of single particle (reflectance). However, unlike the ideal scatter, the real flow particles such as RBCs reflect varying amounts of light depending on their relative angular orientation to the incident beam. Hence, the reflectance in Eq. (8) should be dependent on time: $\alpha = \alpha(t)$. Thus, Eq. (7) can be expressed as

$$
I_{OMAG} = \sqrt{\left[0.89\sqrt{N}\left(\alpha(t) + \alpha(t+\Delta T) \right) \right]\left[1 - \left[\exp\left(-\frac{8}{6}\left(\frac{2\pi}{\lambda_0} \right)^2 \left\langle V^2 \right\rangle \Delta T^2 \right) \right]^{1/2} \times \cos(\Delta\phi(t)) \right]}. \tag{9}
$$

#265340 Received 24 May 2016; revised 15 Jun 2016; accepted 15 Jun 2016; published 20 Jun 2016

With a large *N*, the resultant phasor follows a circular complex Gaussian random distribution [24], and therefore, we can assume that the reflectance $\alpha(t)$ and the phase difference $\Delta\phi(t)$ are also governed by the Gaussian random distribution. Eventually, Eq. (9) indicates that the OMAG signal intensity is related to the number of particles in the imaging voxel and the amplitude decorrelation term consisting of three independent variables: the flow velocity, the time interval, and the wavelength of light source. We expect that with the given wavelength, if the OCT amplitudes are correlated ($0 < g_1(V,\Delta T) < 1$), the OMAG signal power would then represent a product of the particle number and the flow velocity, indicating the total number of particles passing across the voxel cross-section within a unit time, which can be referred to as flux or volumetric flow rate [25]. Otherwise, if the OCT amplitudes are totally decorrelated ($g_1(V,\Delta T) = 0$), the OMAG signal would be saturated for all the velocities beyond the saturation velocity, and its increment would be contributed by only the number of particles in the imaging voxel.

Meanwhile, the particle concentration *C* of the medium is a ratio of a total volume of the particles ($V_{particle}$) to the imaging voxel volume (V_{voxel}). When the shape of particle is assumed to be spherical with a diameter *d*, we can calculate the number of particle *N* by

$$N = \frac{C \cdot V_{voxel}}{\left(V_{particle} = \frac{4}{3}\pi\left(\frac{d}{2}\right)^3 \right)}. \tag{10}$$

Substituting Eq. (10) into Eq. (9) provides a full description of the complex OMAG signal intensity observed at a given concentration as

$$I_{OMAG} = \sqrt{\left[0.89\sqrt{\frac{6C \cdot V_{voxel}}{\pi d^3}} \left(\alpha(t) + \alpha(t+\Delta T) \right) \right] \left[1 - \left[\exp\left(-\frac{8}{6}\left(\frac{2\pi}{\lambda_0}\right)^2 \left\langle V^2 \right\rangle \Delta T^2 \right) \right]^{1/2} \times \cos(\Delta\phi(t)) \right]}. \tag{11}$$

2.2 Numerical simulation of relationship between OMAG signal and flow

With Eq. (11), we numerically simulated the changes in OMAG signal intensity with flow velocity, time interval, and particle concentration. The wavelength was set to 820 nm, equivalent to that of the OCT light source used for flow phantom experiments below. We performed the simulation of multi-velocity scale OMAG for different time intervals with a given particle concentration. To estimate number of particles in the imaging voxel, the imaging voxel was assumed to be a cuboid made by the coherence length of 3 μm (height) and the beam spot size of 10 μm (width), giving a coherent volume of 300 μm^3. The Intralipid particle volume was calculated to be ~0.005 μm^3 with a diameter of 214 nm on average [26]. Therefore, the number of particles in the imaging voxel was estimated to be (cocentration × 300/0.005). Figure 1 shows the simulation result for a 5% Intralipid concentration, where the particle number in the imaging voxel was 3000. It is observed that for each time interval, the OMAG signal intensity increases along with the flow velocity and asymptotically approaches a plateau (~2.8 here). This saturation means that the time separation between the two measurements is too long for the incoming particles to enter and leave the imaging voxel, and the resulting amplitudes would no longer resemble to each other, making the OCT signal completely decorrelated. Since the correlation becomes almost 0 (i.e., the autocorrelation term in Eq. (11) is 0), the OMAG magnitude is saturated for all the velocities beyond the saturation velocity. The longer the time interval, the more the saturation occurs at a relatively slower flow velocity. For example, the signal is almost flattened at 0.2 mm/s for 4 ms, but still increases for 0.1 ms (Fig. 1(b)). Subsequently, it indicates that the OMAG values below the full saturation level are related to the flow velocity, and the saturation level is dictated by

#265340 Received 24 May 2016; revised 15 Jun 2016; accepted 15 Jun 2016; published 20 Jun 2016

the given time interval (1/B-scan rate). Small oscillation in the OMAG magnitude is due to randomness in the two Gaussian random variables, $\alpha(t)$ and $\Delta\phi(t)$ in Eq. (11). Note that at the full saturation level, its randomness is contributed by only the $\alpha(t)$ because the autocorrelation value is 0. Visualization 1 and Visualization 2 visualize the simulated multi-velocity scale OMAG cross-sections of a 5% Intralipid in a microfluidic channel for the time interval of 4 ms and 50 μs, respectively.

Likewise, multi-time scale OMAG by varying flow velocity with the same concentration as Fig. 1 was simulated, the results of which are shown in Fig. 2. Similar to the results in Fig. 1, the OMAG magnitude climbs to its full saturation with its slope much steeper for the faster flow velocity due to the faster decorrelation time. The OMAG magnitudes are fully saturated for all the velocities (0.1 mm/s to 8.0 mm/s) at a time scale beyond 3 ms (~333 Hz), a typical time interval often used for OCTA imaging [19,22,27]. Thus, it is reasonable to conclude that if B-scan rate is below ~333 Hz for OCTA imaging, there does not exist the dependency of OMAG value on the flow velocity that is faster than 0.1 mm/s (saturation velocity). Interestingly, Fig. 3 shows that the magnitude curve (green circles in Fig. 2) increases with the particle concentration (1% to 6%), but the saturation time point remained constant at ~0.2 ms, indicating that the saturated OMAG signal can be increased at all-time scales over the saturation time point with the higher concentration.

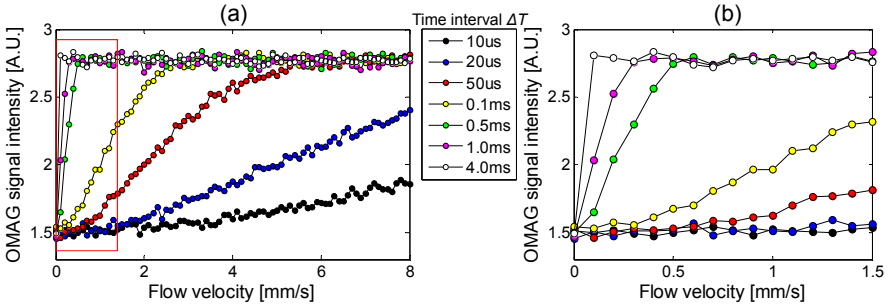

Fig. 1. (a) Numerical simulation of multi-velocity scale OMAG magnitude by varying the values of time interval, probing a scattering medium consisting of 5% Intralipid solution (Visualization 1 and Visualization 2). (b) A zoom-in view of the red box in (a).

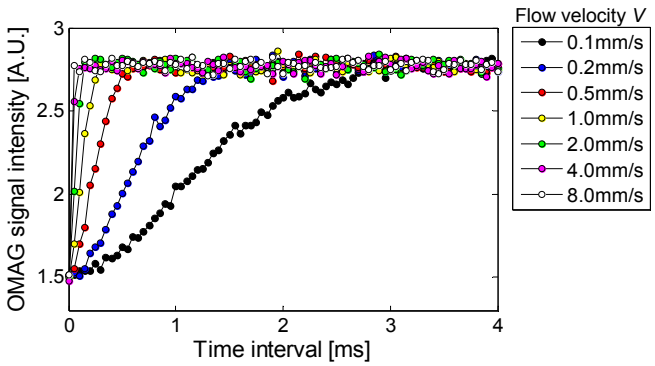

Fig. 2. Numerical simulation of multi-time scale OMAG magnitudes by varying flow velocity at 5% Intralipid.

#265340 Received 24 May 2016; revised 15 Jun 2016; accepted 15 Jun 2016; published 20 Jun 2016

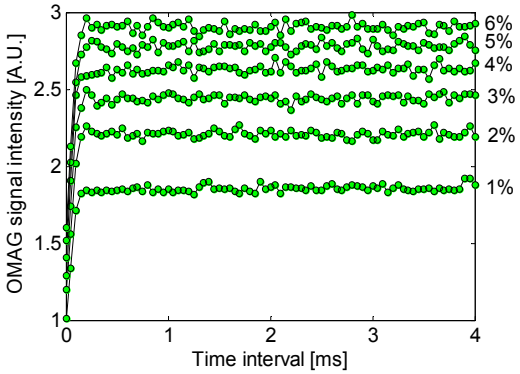

Fig. 3. Numerical simulation of multi-time scale OMAG magnitude by varying particle concentration at the flow velocity of 2.0 mm/s. The full saturation time point is ~0.2 ms.

Furthermore, the dependency of OMAG on particle concentration was examined for the representative time interval of 4.0 ms (Fig. 4(a)) and 0.2 ms (Fig. 4(b)), respectively. In Fig. 4(a), the OMAG signals nonlinearly increase with the concentration but with the same slope for each flow velocity (0.1 mm/s to 8.0 mm/s) examined. This is because the OMAG signal intensity is proportional to a square root of concentration rather than the flow velocity. Since the autocorrelation is 0 for this case, only the concentration contributes to the variation in the OMAG magnitude. On the other hand, at the time interval 0.2 ms (Fig. 4(b)), there was significant difference in the slopes. This is because the OCT amplitudes still remained correlated with the rest of flow velocities except for 2.0~8.0 mm/s, and the respective OMAG signals increased with both concentration and flow velocity. Visualization 3 visualizes the simulated multi-concentration scale OMAG cross-sections of an Intralipid particle in the microfluidic channel for the flow velocity of 2.0 mm/s and at time intervals of 4.0 ms.

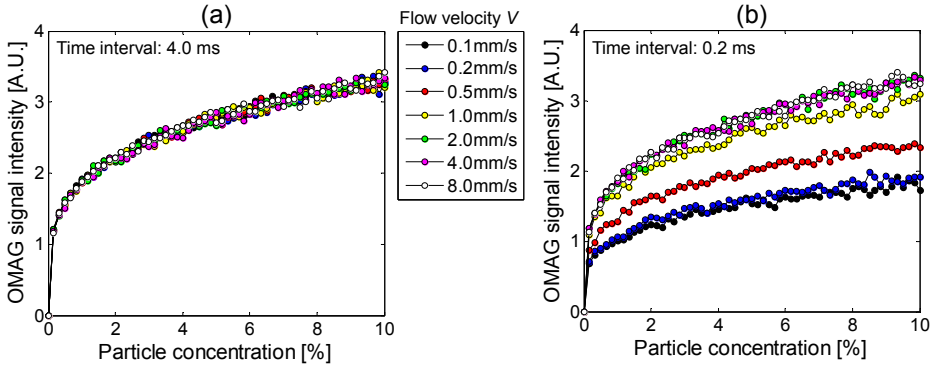

Fig. 4. Numerical simulation of multi-concentration scale OMAG magnitude by varying the flow velocity at the time interval of (a) 4.0 ms and (b) 0.2 ms, respectively (Visualization 3).

3. Materials and methods

3.1 System set-up

In order to validate the simulation results in Sec. 2, we performed microfluidic flow phantom experiments using a custom OCT device and the OMAG technique. The OMAG based OCT imaging system is schematically shown in Fig. 5(a), that has been described previously [28]. In brief, the light source was a SuperK Versa supercontinuum laser (Koheras A/S, Denmark) pumped by an Nd:YAG laser, providing a broadband output spectrum with a center wavelength of 820 nm and a spectral bandwidth of 120 nm. The light was launched into a

#265340 Received 24 May 2016; revised 15 Jun 2016; accepted 15 Jun 2016; published 20 Jun 2016

fiber-based spectral domain OCT (SD-OCT) interferometer. In the sample arm, a 10 × objective lens (LSM02-BB, an effective focal length = 18 mm, Thorlabs, New Jersey) was used as a scan lens that focused the collimated beam onto a flow channel in a microfluidic chip driven by a syringe pump (Harvard Apparatus PHD ULTRA, Massachusetts). The optical power of the beam illuminating on the microfluidic chip was measured to be ~3 mW. The lights retro-reflected from the reference mirror and backscattered from the sample were recombined and formed spectral interferograms that were subsequently received by a home-built high-speed spectrometer, giving a maximum line-scan rate of 140 kHz. At this A-scan rate, the sensitivity of the system was measured at ~98 dB around the zero delay line and fell off to 70 dB at ± 3 mm position. The lateral resolution was ~9 μm that was measured with a minimum detectable line pair of a USAF resolution target image. The measured axial resolution was ~3 μm in air. For the flow phantom imaging, water-diluted Intralipid solution was employed to perfuse the microfluidic channel and provide the OMAG flow signal. The microfluidic chip on the sample stage was slightly tilted (20°) along the channels to avoid hyper-reflection from the flat surface of the chip during imaging (Fig. 5(b)). Details of the microfluidic chip are described in Sec. 3.3.

3.2 Scanning protocol

For OMAG data collection, we used an M-B mode (repeated B-scan) protocol. Briefly, in the fast scan (X) direction, 400 A-lines were captured to compose one B-scan cross-section. Each B-scan covered a range of 2.3 mm in the X-direction with a 5.8 μm spacing between the adjacent A-lines. In the slow scan (Y) direction, the Y-axis galvo scanner was fixed, and 200 repeated B-frames were captured at one transverse position of the microfluidic channel. All measurements were performed at a B-scan acquisition speed of 250 frame/s corresponding to an inter-frame time interval of 4 ms.

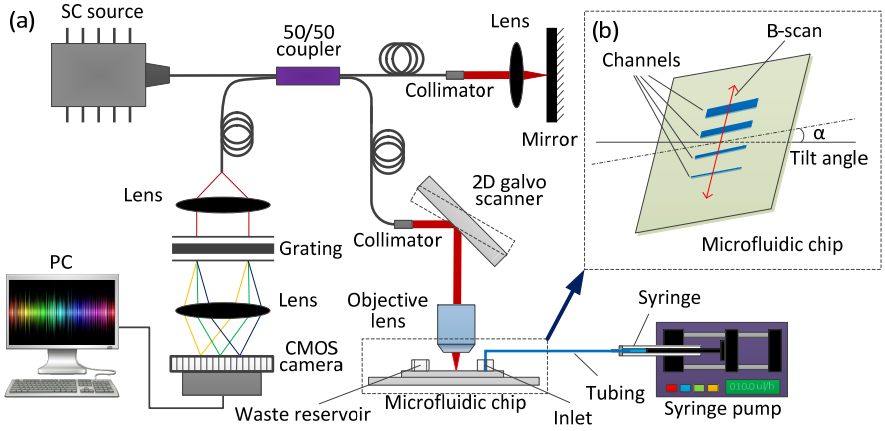

Fig. 5. (a) Schematic of a home-built spectral domain OCT (SD-OCT) system. SC source, supercontinuum laser. (b) Illustration of the sample placement and scan direction. The microfluidic chip is slightly tilted (α = 20°) toward the sample plane to prevent hyper-reflection from the flat surface of the chip.

3.3 Design and fabrication of microfluidic chip

The microfluidic channels were used to mimic single blood vessels through which 5% Intralipid solution was perfused to simulate the moving particles that give the OCT scattering signals. The microfluidic chip utilized in this study is schematically illustrated in Fig. 6. Figure 6(a) shows the microfluidic channel layout: at each branching point, a higher-order channel splits into two lower-order channels with the half-width of the higher-order channel. Fluid enters the microfluidic chip through the inlet and flows into the first-order channel. The

#265340 Received 24 May 2016; revised 15 Jun 2016; accepted 15 Jun 2016; published 20 Jun 2016

width of the first-order channel is 240 μm, followed by the second-order channel, 120 μm; the third order, 60 μm; the fourth order, 30 μm; and the fifth order 15 μm. After the 15 μm channels, the bottom half is symmetrical to the top half. This layout mimics the vascular network: the top half is equivalent to the arterial-end system including higher-order arteries, intermediate-order arterioles and lower-order capillaries, followed by the venous-end system with intermediate-order venules and higher-order veins. Moreover, the symmetric design provides an important feature in the flow-field distribution, which is a constant average flow velocity throughout the microfluidic channels. Such design facilitates the comparison of OMAG signals in channels of different size with the same flow velocity, which can be done with one single experiment. We consider the channel size a potential determinant factor of OMAG signal intensity because it has been demonstrated to contribute significantly to laser speckle angiography [29]. Comparison of multiple channel sizes in a single experiment can minimize systemic errors caused by variance in experimental conditions. Figure 6(b) is a zoom-in view of the region of interest (ROI) that is highlighted by the dashed box in Fig. 6(a). It covers an area of 2×2 mm^2. Figure 6(c) schematically illustrates a cross-section of the microfluidic channel at the location of the M-B frame acquisition as indicated by the red line in Fig. 6(b). The channel body was fabricated with Polydimethylsiloxane (PDMS) mixed with TiO_2 powder to mimic static tissue surrounding blood vessels. Four channels with the same height (40 μm) but different widths, 15 μm (named C1), 30 μm (C2), 60 μm (C3) and 120 μm (C4), were covered in the cross-section.

The microfabrication procedure of the microfluidic chip is briefly described as follows: 1) design of the photomask: 2D chip design was drawn with SolidWorks software containing fluidic structure to be transferred to PDMS, and a monochrome photomask was commercially printed with high resolution. 2) Fabrication of the microfluidic channel mold: A mold was produced by patterning SU8 epoxy-based photoresist on a silicon substrate using standard photolithography techniques. 3) Molding and sealing the microfluidic channel: A mixture of 1.8 mg of TiO_2 per gram of PDMS was poured over the mold and cured at 95 °C for 1 hour. It was then peeled off from the mold, creating an inverted cast in PDMS of the mold. Micro-punches with diameters of 1.2 mm and 4 mm were used to punch the inlet hole and the outlet waste reservoir, respectively. The inlet hole was slightly smaller than the tubing size (1.59 mm OD, PEEK tubing, IDEX, Lake Forest, IL) to ensure a good seal. Finally, the molded PDMS was bonded with a glass slide irreversibly through surface treatment of air (oxygen) plasma. Since the PDMS layer is very thin (~1 mm thickness), two additional thick PDMS bulks punched with 1.2 mm and 4 mm holes were bounded with the channel body at the inlet and outlet, respectively (see Fig. 6(d)). This further secured the inserted tubing in the inlet and enlarge the capacity of the outlet reservoir.

#265340 Received 24 May 2016; revised 15 Jun 2016; accepted 15 Jun 2016; published 20 Jun 2016

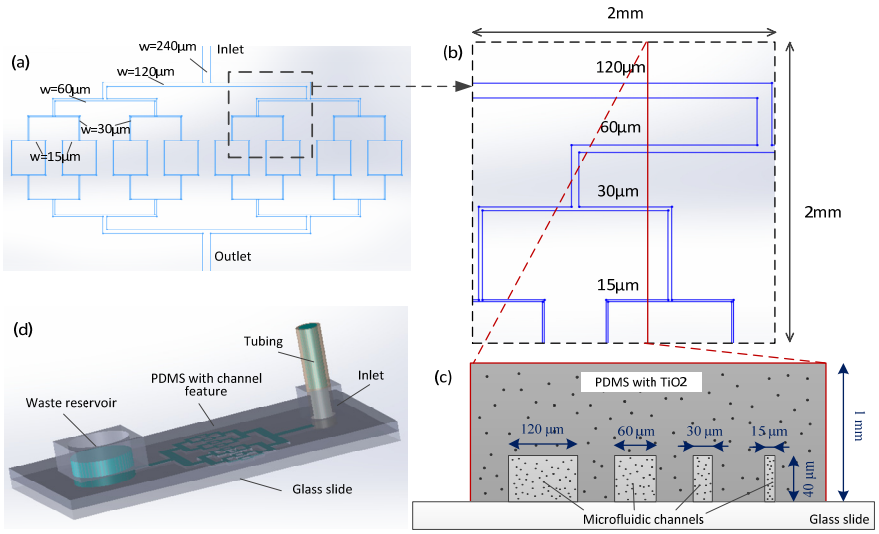

Fig. 6. Illustration of the microfluidic chip design. (a) Layout of the microfluidic channel. A dashed box highlights the region of interest. (b) Enlarged view of the region of interest (2 × 2 mm^2). Four different dimensions of channels are included in the region: 120 μm, 60 μm, 30 μm, and 15 μm wide. The solid red line indicates the B-frame location of M-B mode scans to collect OMAG data. (c) Schematic of the cross-section at the location of the red solid line in (b). (d) Diagram of the fabricated microfluidic chip.

3.4 Evaluation of OMAG signal intensity in the microfluidic chip

A 2D map of the channel network was first generated by maximum intensity projection (MIP) of a 2D OMAG scan to localize the B-frame location for examination as shown in Fig. 7(a). The 5% Intralipid solution was used to provide OMAG contrast. Unlike the scanning protocol described in Sec. 3.2, the scanning for the 2D map consisted of 5 repeated B-scans at 400 spatial locations (C-scan), covering a 2 × 2 mm^2 field of view (the area of Fig. 6(b)). A blue line was drawn across the center of Fig. 7(a), which indicates the B-frame location for subsequent examination of the OMAG signal relationship with flow. Note that the OMAG signal near the blue line is apparently stronger compared to the top and bottom areas. This is because of the tilted sample where the middle area in Figure was in focus. The purpose of having a 2D map was to ensure that the target B-frame location would not be too close to any corner of the microfluidic channels, where possible turbulent flow may occur. Figure 7(b) is the mean image of OMAG cross-sections produced with 200 repeated OCT B-scans at the location indicated by the blue line in Fig. 7(a). Five windows (green dashed boxes, 50 × 40 pixels in size) were selected to measure OMAG intensity from each OMAG cross-sectional images: C1 (covering the 15 μm channel), C2 (the 30 μm channel), C3 (the 60 μm channel), C4 (the 120 μm channel), and N (a flow-free region, representing the background noise). Figure 7(c) is an *en face* MIP image of the repeated OMAG cross-sections of Fig. 7(b). Qualitatively, OMAG signal intensity fluctuation can be observed in each channel over time.

#265340 Received 24 May 2016; revised 15 Jun 2016; accepted 15 Jun 2016; published 20 Jun 2016

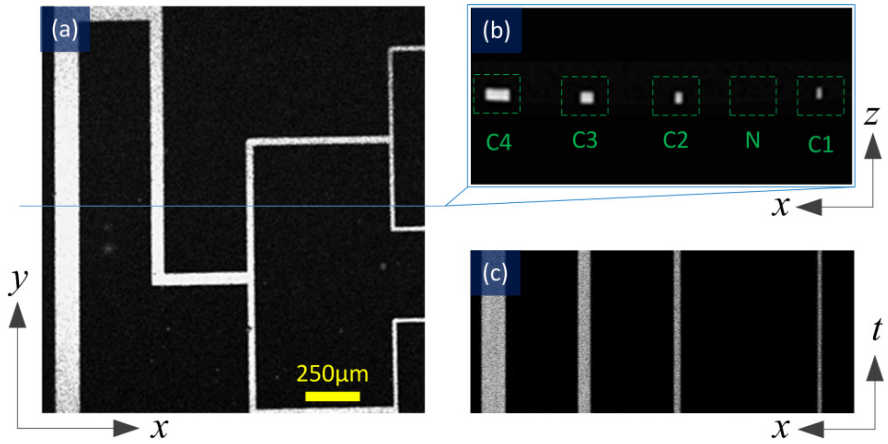

Fig. 7. OMAG images of the microfluidic chip perfused with 5% Intralipid solution. (a) *En face* MIP image of the region of interest (Fig. 6(b)). (b) Mean image of OMAG cross-sections produced with 200 repeated OCT B-scans at the location indicated by the blue line in (a). Green dashed boxes highlight five areas used to calculate OMAG intensity. C1: channel 1 (15 μm); C2: channel 2 (30 μm); C3: channel 3 (60 μm); C4: channel 4 (120 μm); N: background noise. (c) *En face* MIP image of the repeated OMAG cross-sections, i.e., MB scan.

Because the complex OCT signal is usually described as the addition of static and dynamic scattering components and additive noise within a single imaging voxel [30], the resulting complex OMAG signal can be subject to noise. Therefore, it is necessary to exclude the noise from the OMAG signal for reliable quantification. We compensated for the OMAG signal intensity by eliminating the noise signal as

$$I(C_i) = \frac{\sum_{C_i} I(x_i, z_i) - \sum_N I(x_N, z_N)}{A_i}. \quad (12)$$

where (x_i, z_i) are the coordinates of pixels within the C_i box (i = 1,2,3,4), and (x_N, z_N) are the coordinates of pixels within the N box. I denotes a pixel intensity value in the OMAG cross-section. A_i is the relative value of the each channel cross-sectional area i, giving A_1 = 1, A_2 = 2, A_3 = 4, and A_4 = 8. The cross-section ratio of the channels equals their width ratio because they have the same height (40 μm). To get better image quality, usually, an OMAG image is produced with an empirical threshold to clean up noise signals below the threshold, followed by normalizing all pixels to a range from 0 to 1. However, for most cases, a higher threshold is required to completely eliminate the noise signal, which may also remove a portion of the weak signal from the flow, leading to underestimation of OMAG intensity. Here, to preserve the entire flow signal for OMAG evaluation, we utilized a zero threshold in the processing algorithm. In this case, subtraction of noise background from the signals of channel areas using Eq. (12) is a good approach for accurate quantification that needs to be independent of the subjective thresholding. This can be illustrated with Fig. 8. Figures 8(a)-8(e) are cross-sectional OMAG images of the microfluidic channels processed with five different thresholds, representing 0%, 2%, 5%, 8%, and 12% of the maximal intensity level, respectively. Comparing the enlarged images (shown in Figs. 8(f) and 8(g)) of the green box in Fig. 8(a) and the red box in Fig. 8(e), one can identify the difference in the noise signal. Figure 8(g) exhibits a clean background, while Fig. 8(f) appears noisier. We quantified the OMAG intensity of boxes C1 and N under different thresholds as an example, and displayed the results with a bar chart in Fig. 8(h). Sum_{C1} and Sum_N denote summation of pixel values within C1 and N boxes, respectively, and (Sum_{C1} - Sum_N) is the difference between the two summation values. All values used in Fig. 8(h) are averaged from all the measurements. As

#265340 Received 24 May 2016; revised 15 Jun 2016; accepted 15 Jun 2016; published 20 Jun 2016

expected, a lower threshold yielded higher intensity in both C1 and N areas. Because the measurement of C1 area itself is highly dependent on the processing threshold, it cannot stand for the actual OMAG signal of Channel 1. By contrast, (Sum_{C1} - Sum_N) remains relatively constant for all the five thresholds, and is therefore a more accurate representation of the OMAG signal of Channel 1. Once the noise-free OMAG signal is divided by a normalized channel cross-sectional area as described by Eq. (12), an average OMAG intensity of the channel is obtained. As aforementioned, the excessive thresholding not only removes noise, but also a large portion of the OMAG signal, making the OMAG signal close to the noise floor. This is why (Sum_{C1} - Sum_N) starts to slightly decrease when the threshold is higher than a certain level.

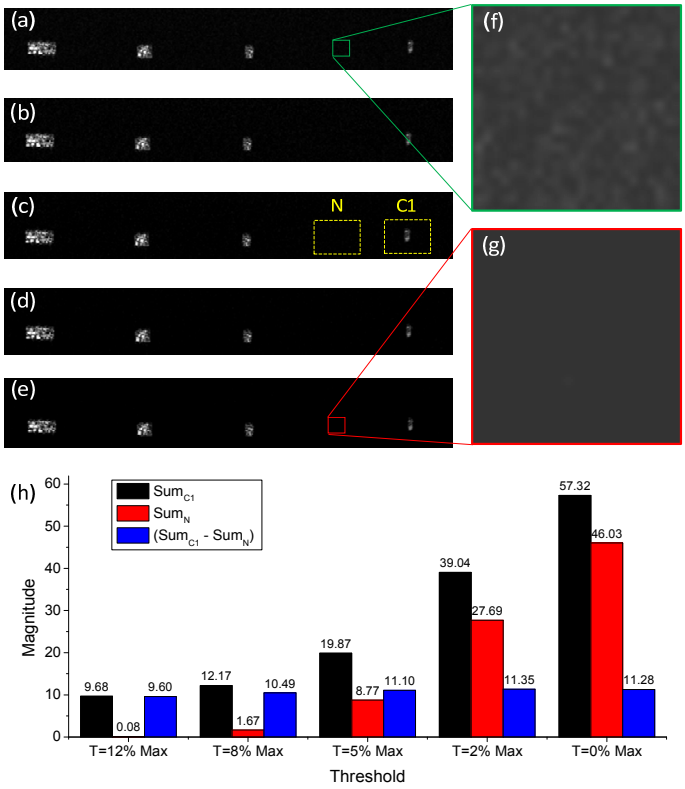

Fig. 8. Comparison of OMAG images and intensity quantifications under different processing thresholds. (a)-(e) Cross-sectional OMAG images processed with the thresholds (a) 0%, (b) 2%, (c) 5%, (d) 8%, (e) 12% of the maximal intensity level. (f) and (g) are zoom-in views of the green box in (a) and the red box in (e), respectively. (g) Quantification of OMAG intensity in C1 and N windows under each threshold.

3.5 Settings of the syringe pump

The flow of Intralipid in the microfluidic channel was driven by an external syringe pump. Since the channel design was based on a dimidiate and symmetric strategy, the flow parameters in each sub-channel were predictable. This facilitated the examination of the relationship between the OMAG signal and flow parameters such as velocity, flow, flux, and channel size. Table 1 lists the predicted flow rate and average velocity in each of the four channels under different settings of the pump rate adopted in our flow phantom experiment. In addition, flux is also predictable as it is the product of velocity and particle concentration.

#265340 Received 24 May 2016; revised 15 Jun 2016; accepted 15 Jun 2016; published 20 Jun 2016

4. Experimental results

4.1 Examination of the microfluidic chip

Before we collected OMAG data with the microfluidic phantom, we performed COMSOL simulation and Doppler OCT imaging on the microfluidic chip to validate if the calculation of flow parameters in Table 1 is reliable. COMSOL simulation results, as shown in Fig. 9, predict the same flow velocity scale in the four channels with different sizes. The images exhibit flow velocity distribution of the channel at the center layer in depth. Under a pump flow rate of 34.56 μL/hr, theoretically, the average flow velocity is 1 mm/s in each channel. Due to the 2D parabolic profile of the flow field in the channels, velocity at the center streamline of the center layer in each channel (~1.8 mm/s) is higher than the average velocity.

Table 1. Settings of the pump rate and corresponding flow rate and average velocity in the four channels

Pump rate (μL/hr)	Flow rate(μL/hr)				Average velocity(mm/s)			
	C1	C2	C3	C4	C1	C2	C3	C4
17.28	8.64	4.32	2.16	1.08	0.5	0.5	0.5	0.5
34.56	17.28	8.64	4.32	2.16	1.0	1.0	1.0	1.0
51.84	25.92	12.96	6.48	3.24	1.5	1.5	1.5	1.5
69.12	34.56	17.28	8.64	4.32	2.0	2.0	2.0	2.0
86.4	43.2	21.6	10.8	5.4	2.5	2.5	2.5	2.5
103.68	51.84	25.92	12.96	6.48	3.0	3.0	3.0	3.0
120.96	60.48	30.24	15.12	7.56	3.5	3.5	3.5	3.5
138.24	69.12	34.56	17.28	8.64	4.0	4.0	4.0	4.0
155.52	77.76	38.88	19.44	9.72	4.5	4.5	4.5	4.5
172.8	86.4	43.2	21.6	10.8	5.0	5.0	5.0	5.0
190.08	95.04	47.52	23.76	11.88	5.5	5.5	5.5	5.5
207.36	103.68	51.84	25.92	12.96	6.0	6.0	6.0	6.0
224.64	112.32	56.16	28.08	14.04	6.5	6.5	6.5	6.5
241.92	120.96	60.48	30.24	15.12	7.0	7.0	7.0	7.0
259.2	129.6	64.8	32.4	16.2	7.5	7.5	7.5	7.5
276.48	138.24	69.12	34.56	17.28	8.0	8.0	8.0	8.0

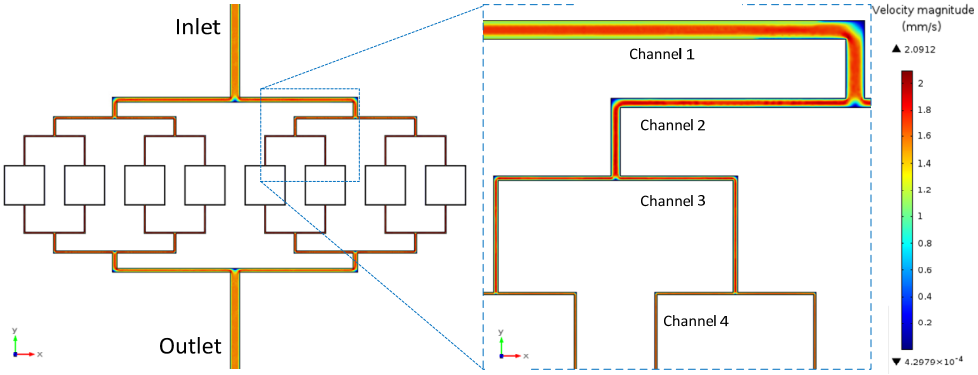

Fig. 9. COMSOL simulation of the microfluidic channel under the pump rate of 34.56 μL/hr. Left panel: flow velocity distribution in the full channel network. Right panel: zoom-in view of the flow velocity distribution in the region of interest.

Many factors can affect flow performance of the microfluidic chip: errors in the microfabrication procedure, dirt inside channels, uneven channel walls, etc. Simulation was performed under ideal conditions, and in experiments, the same performance may not be guaranteed. Therefore, M-B mode Doppler OCT imaging of the four channels was performed at the same B-scan location of Fig. 7(b) to experimentally examine the microfluidic chip. In

#265340 Received 24 May 2016; revised 15 Jun 2016; accepted 15 Jun 2016; published 20 Jun 2016

this measurement, the number of A-lines/B-scan was increased to 600. Figure 10(a) is an enface maximum projection view of color-coded axial velocities calculated from the Doppler OCT signals of the four flow channels with a theoretical average flow speed of 1mm/s. The absolute values of axial velocity distribution along the x-axis were averaged along the time-axis and plotted in Fig. 10(b). The four equal peaks in Fig. 10(b) demonstrate the same flow velocity in the four channels, which confirms the COMSOL simulation results.

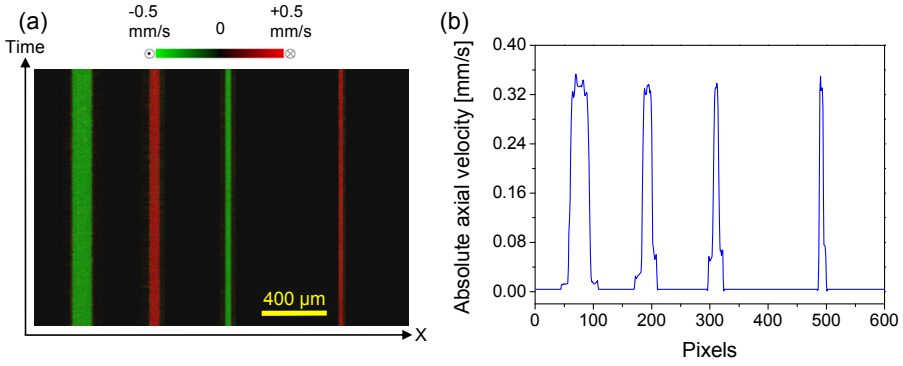

Fig. 10. M-B mode Doppler OCT imaging results of the four channels. (a) Enface maximum projection color map of the axial velocities calculated by Doppler OCT signals of the four flow channels. Color bar: range of axial velocity; green and red colors represent upward and downward flow, respectively. (b) Profile of absolute values of the axial velocity distribution along the x-axis that were averaged along the time-axis.

4.2 Relationship between the OMAG signal and the flow velocity

According to the simulation results in Fig. 1, OMAG magnitude has a linear relationship with flow velocity within a certain velocity range that is dependent on the OCT B-scan rate. When the time interval between adjacent B-frames is 50 μs, the OMAG signal is approximately linear to flow velocity ranging from 0.3 to 4 mm/s. It covers a typical blood flow velocity range of capillaries in the tissue beds. If the time interval is even shorter, the linear range can be expanded to a faster velocity. However, our current imaging setup worked at a B-frame rate of 250 Hz, corresponding to a frame interval of 4 ms, much longer than 50 μs. Therefore, it was expected that the dependence of OMAG magnitude on velocity would be saturated beyond 0.1 mm/s (see Fig. 1(b)). To validate this prediction and examine the OMAG dependence on velocity under a 250 Hz frame rate, we collected data at the 16 pump rates listed in Table 1 from 17.28 μL/hr to 276.48 μL/hr, covering a flow velocity range from 0.5 mm/s to 8 mm/s. 5% Intralipid was used in this experiment.

Figure 11 shows the statistical measurements of the OMAG signal in the four channels under different flow velocities. Mean values and standard deviations were calculated from all measurements for each channel. As can be seen from Fig. 11, OMAG signals in all the four channels randomly oscillated near at a saturation level. The trends of the oscillation in the four channels were not in consistency and also random. This demonstrates that, at this frame rate (250 fps), OMAG intensity has little relationship to flow velocity, which confirms our simulation results.

#265340 Received 24 May 2016; revised 15 Jun 2016; accepted 15 Jun 2016; published 20 Jun 2016

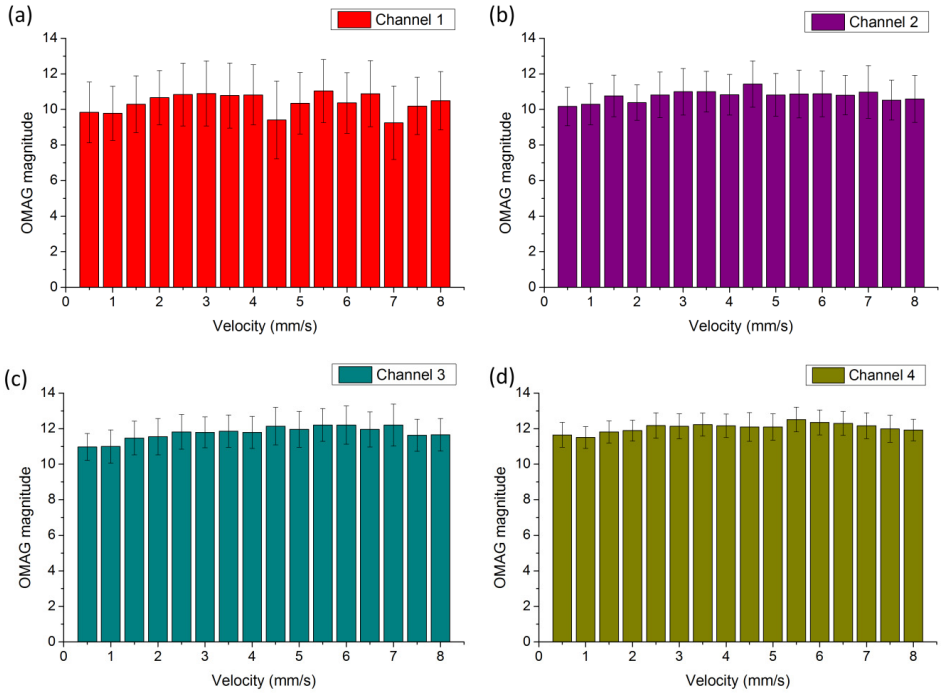

Fig. 11. Statistic measurements of the OMAG signal in the four channels at different flow velocities: (a) channel 1 (15 μm width); (b) channel 2 (30 μm width); (c) channel 3 (60 μm width); (d) channel 4 (120 μm width).

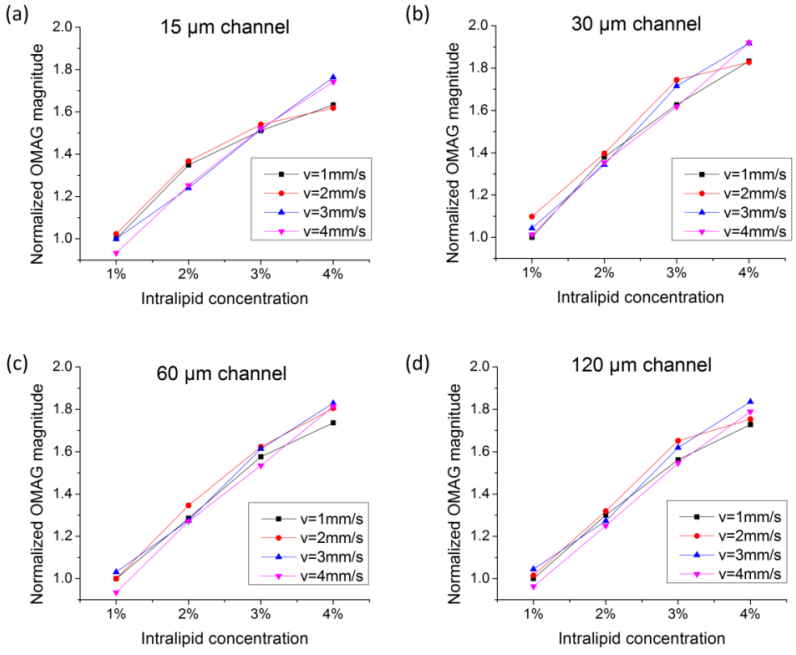

Fig. 12. Quantification of OMAG intensity produced by different concentrations of Intralipid solution in (a) channel 1, (b) channel 2, (c) channel 3, (d) channel 4, at different pump rates.

#265340 Received 24 May 2016; revised 15 Jun 2016; accepted 15 Jun 2016; published 20 Jun 2016

4.3 Relationship between the OMAG signal and the perfusate concentration

According to the simulation results in Fig. 4, the particle concentration of the perfusate is a major determinant of OMAG intensity. In order to validate this prediction, we experimentally examined the OMAG signal of the four channels at different Intralipid concentrations. At constant pump rates, 34.56 μL/hr, 69.12 μL/hr, 103.68 μL/hr, and138.24 μL/hr (corresponding to flow velocity 1 mm/s, 2 mm/s, 3 mm/s, and 4 mm/s, respectively), OMAG data were collected with 4 Intralipid concentrations at 1%, 2%, 3%, and 4%. The measured results were all normalized to the OMAG magnitude of 1% Intralipid and are statistically shown in Fig. 12, in which all data points are mean values of the measurements. Consistently, the OMAG signal of each channel size at each flow velocity increased as the Intralipid concentration increased. The overall trend suggested by the curves was that the increase of OMAG magnitude between 1% and 2% Intralipid concentrations was more dramatic than that between 3% and 4%. The trend is regarded as a slight deviation from linearity because of the square root of particle number in Eq. (11). These quantification results demonstrate the dependence of the OMAG signal on perfusate concentration as predicted by the simulation.

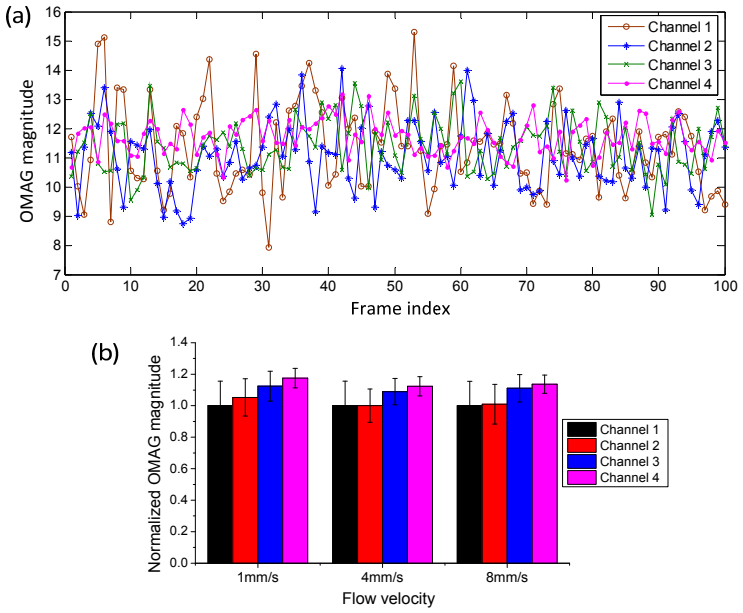

Fig. 13. (a) OMAG signal intensity of the four channels in 100 consecutive cross-sections at the same frame location (pump rate = 34.56 μL/hr). (b) Comparison of normalized OMAG intensity in the four channels under different pump rates corresponding to flow velocities 1 mm/s, 4 mm/s and 8 mm/s. Mean and standard deviation were calculated from all measurements.

4.4 Relationship between the OMAG signal and the channel size

Our previous experience with *in vivo* microvascular imaging suggests that the big blood vessels appear noticeably brighter than the small capillaries in the OMAG images [19,31]. This raises a question: whether or not the OMAG signal intensity is dependent on the vessel size. In order to investigate this question, we examined the OMAG signal intensity of the four channels (1:2:4:8 ratio in channel width) perfused with 5% Intralipid solution. Figure 13(a) shows the OMAG signal intensity fluctuation in the four channels over 100 frames at the same location (pumping rate = 34.56 μL/hr). The temporal traces of the four groups of data points reveal random signal oscillation in all four channels at a similar level such that channels cannot be distinguished from one another. We also statistically compared the

#265340 Received 24 May 2016; revised 15 Jun 2016; accepted 15 Jun 2016; published 20 Jun 2016

OMAG signal intensities between the four channels at the pump rates of 34.56 μL/hr, 138.24 μL/hr, and 276.48 μL/hr, corresponding to flow velocities of 1 mm/s, 4 mm/s, and 8 mm/s, as shown in Fig. 13(b). The OMAG signal intensity of each channel was normalized to the intensity of Channel 1. As can be seen from the bar chart, although channel size varies significantly among the four (up to 700% in difference), no significant difference between their OMAG signals was found (less than 20%) regardless of the pump rates. This demonstrates that the OMAG signal is not determined by channel size. A larger channel may produce a stronger OMAG signal due to the greater number of particles, leading to 1) higher overall reflectance, and 2) more multiple scattering events [29].

5. Discussion

5.1 Validation of analytical model

The numerical simulation results of the analytical model showed the dependency of the OMAG signal on the various flow measures, Figs. 1–4. In Fig. 1, for each time interval, the OMAG magnitude was rather linear to a specific range of velocity, defined as an operating range. The linearity did not hold for the velocity that is above the operating range where the OMAG signal became constant for all velocities beyond a saturation velocity. The signal saturation was identified from the flow phantom experiments. Table 2 shows short time interval-saturation velocity pairs calculated from our model. Surprisingly, the simulated values were almost consistent with the results from flow phantom experiments with a split-spectrum amplitude-decorrelation angiography (SSADA), one of the intensity decorrelation-based OCTA [32]. In the experiment, the authors used an 840 nm SD-OCT set-up similar to our system and a glass capillary tube with an inner diameter of 200 μm as a flow phantom. M-mode measurement was made on the capillary tube using the SSADA algorithm [32]. Therefore, we can conclude that the OMAG delivers result that has relationship with the amplitude decorrelation, a common practice of dynamic light scattering inversion techniques [29], and its measurable velocity range (operating range) for velocity quantification is strictly dependent on the OCT B-scan rate that is employed.

However, our work showed another notable relationship: the nonlinear tendency of OMAG value with the particle concentration, Fig. 4. This signal trend was also validated with the phantom experiment albeit at the limited range of concentration (1~4%). It indicates that the higher concentration would be able to readily increase the saturated OMAG signal. Therefore, our OMAG model is reasonable and supports our hypothesis that a OMAG signal is related to the flux (concentration × flow velocity), which is however valid only within the operating range.

Table 2. Simulated time interval-saturation velocity pairs (λ: 820 nm, Concentration: 5%)

Time interval (ms)	Saturation velocity (mm/s)
0.05	7.5
0.11	3.7
0.16	2.6
0.22	1.8
0.28	1.3

5.2 Comparison with previous works

Other OCT groups performed similar flow phantom studies for quantification of OCTA signals computed with different amplitude decorrelation-based algorithms [32,33]. Liu *et al*. analyzed features of intensity-based Doppler variance (IBDV) method with several flow parameters (sampling density, time interval and flow velocity) [33]. In the work, M-mode measurements were made on a 0.1% Intralipid solution flowing through a 500-μm-diameter

#265340 Received 24 May 2016; revised 15 Jun 2016; accepted 15 Jun 2016; published 20 Jun 2016

capillary tube embedded in a tissue phantom [33]. As mentioned in Sec. 5.1, Tokayer *et al*. have performed *in vitro* phantom study using whole human blood to investigate the effect of flow velocity on SSADA signal [32]. Typically, their phantom results were similar to our simulation and experimental ones regarding relation of the OCTA signals to flow velocities for different time intervals. This is true because the OMAG signal is involved with the amplitude decorrelation like IBDV and SSADA. Unlike the IBDV and SSADA, however, the OMAG is also dependent on the particle concentration, which distinguishes the flow relationship from their results. It is unclear if the IBDV or SSADA has such concentration dependency because the related study was not done in their phantom works. In this way, our study is helpful to explain modulation in the OCTA signal of vascular tissues exposed under various physiological challenges such as systemic hyperoxia [34] or visual stimulation [35]. For example, it was reported that the excessive oxygen inhalation in mice leads to an increase in the OMAG signal at cortical capillary vessels [34]. For the B-scan rate of 280 Hz (time interval of 3.6 ms), the saturation velocity is ~0.3 mm/s. Since RBC speeds in the capillaries of rodent cerebral cortex are mostly ranged from 0.5~2.0 mm/s [36], the measured OMAG signal should have been saturated at the smallest vessels, but it was not. This discrepancy of long standing concern is raised by decorrelation-based OCTA measurements including OMAG [32]. Given our analytical model and experiments, we speculate that hyperoxia may increase cerebral blood flow (CBF) at the capillaries, where an increase in CBF is associated with increased RBC speed and hematocrit in the capillaries. For the time interval (3.6 ms), rather than the RBC speed, the hematocrit may become a dominant flow metric to increase the OMAG signal. Indeed, the increased CBF may reduce the long latency between the single-file flowing RBCs through the capillary because of the higher hematocrit, increasing the number of RBCs in the imaging voxel (i.e., the increase in concentration).

5.3 Limitation of this work

There are a few limitations of our current work. First, in the analytical model, we did treat the detected OCT signal as a sum of the single-scattering light fields reflected from the individual particles. In scattering media such as turbid tissue, however, light goes through tremendous scattering events as it propagates through the tissue to the sample volume, scatters back, and then propagates once again through the tissue back to the lens. Therefore, the real OCT signal should be described as a superposition of all the backscattered light fields which undergo single or very little scattering and multiple scattering in spite of its short coherence gating and confocal optics in signal detection [37]. This multiple scattering effect was not reflected in our model because of its complexity. This is the reason we could not simulate the effect of flow channel size on the OMAG signal, where the little increase in OMAG signal was experimentally observed from the wider channel at the same concentration. The increase might be due to mutual interference among the multiple scattered light fields.

Second, the results from flow phantom work may not be valid for high resolution OMAG *in vivo*. The intralipid solution used is composed of particles with a few hundred nm in diameter, much smaller than the human RBC size of ~7 μm. Because the RBC diameter is comparable to or bigger than the imaging voxel size determined by the OCT probe optics, the contribution of particle concentration in the single voxel may be marginal or negligible for *in vivo* imaging using the high magnification OCT system.

5.4 Relationship between OMAG and retinal blood flow

Being able to measure and quantify retinal blood flow will help clinicians gain more insight into the physiology of a retinal vascular bed. Quantitative assessment of the retinal microvasculature may provide more information about vascular pathology in ocular tissues because in ocular diseases, the earliest anomalies may arise in the microvasculature. At present, there is no standard method available to accurately quantify the retinal blood flow. Clinically, fluorescein angiography (FA) and indocyanine green angiography (ICGA) are the

#265340 Received 24 May 2016; revised 15 Jun 2016; accepted 15 Jun 2016; published 20 Jun 2016

standard procedures for examining blood flow of the retina and choroid using contrasting dyes. However, their use is limited to qualitative analysis of the pictured vessel morphology. Some optical imaging methods such as laser Doppler flowmetry, laser speckle flowgraphy, Doppler OCT have been used to directly measure the total or mean retinal blood flow, blood volume, and velocity [38–40]. More recently, OCTA has been used to indirectly assess the retinal blood flow using single quantitative indices that parameterize flux, vessel area density, and non-perfusion area with the acquired OCT angiograms [41–43]. While promising, they have not yet become a clinically acceptable tool for the blood flow assessment. In this work, we investigated the quantitative relationship of the OMAG signal to flow with the vessel-like scattering flow phantom. The OMAG signal is a product of the velocity of the particle and its concentration, or density, distributed in the imaging voxel, which indicates a concept of flux, and therefore can be further referred to provide the volume or perfusion information of the retinal tissue. The volume of the retinal blood flow suggests how much blood flow is needed for a specific tissue, and thus may indicate any changes or defects of the tissue even before any functional or structural defects can be physically detected. The clinical OMAG scan protocol previously published by our group was a repeated B-mode scan, and the time separation between the consecutive B-scans was 3.8 ms, corresponding to 263 frames/s [20,44]. At this time scale, the saturation velocity is smaller than 0.3 mm/s for a center wavelength of 840 nm of the SD-OCT system used for the retinal OCTA imaging. Considering the RBC speeds of normal human retinal capillaries ranged from 0.3 to 3.3 mm/s [45], the OMAG signal could be saturated even at the smallest vessels. Although the relationship between the OMAG signal and the flow velocity can easily plateau for the current clinical setting, the magnitude of OMAG signal with concentration (particle density) shows a linear correlation as shown in Fig. 12. It is still encouraging that the amplitude of the OMAG signal may be a good indicator of the perfusion of the retinal blood flow and enables the quantification of retinal blood flow. The easily saturated relationship between the OMAG signal and flow velocity may be resolved by using an M-mode scan protocol that repeatedly captures A-lines with a much shorter time interval with the current OCT system, or alternatively, using an ultrafast OCT system that can provide a much shorter inter-frame time interval.

6. Conclusion

In summary, we have attempted to establish a quantitative relationship between OMAG and vascular flow. To examine our hypothesis that the OMAG is dependent on a flux of blood flow, the OMAG signal has been analytically modeled and numerically simulated in the proposed model. The microfluidic flow phantom experiment has been performed to validate the simulation results. We conclude that the OMAG signal is a function of flux within a specific velocity range entirely limited by a time scale of OMAG measurement and beyond the velocity range, OMAG is proportional to the particle concentration. With the current formulation of OCTA methodology, the use of the M-mode scan [46] or MHz OCT [47] would be necessarily for comprehensive assessment and accurate quantification of retinal blood flow from the measured OCTA signals.

Acknowledgments

This work was supported in part by grants from the National Heart, Lung, and Blood Institute (R01HL093140) and the National Eye Institute (R01EY024158). The content is solely the responsibility of the authors and does not necessarily represent the official views of grant giving bodies.